JOURNAL OF GEOPHYSICAL RESEARCH, VOL. 104, NO. C9, PAGES 21,123–21,136, SEPTEMBER 15, 1999

Frictionally modified flow in a deep ocean channel: Application to the Vema Channel

Johann H. Jungclaus and Michael Vanicek

Institut für Meereskunde an der Universität Kiel, Kiel, Germany

Abstract. The modification of the exchange flow in a deep southern hemisphere passage, resembling the Vema Channel, by frictionally induced secondary circulation is investigated numerically. The hydrostatic primitive equation model is a two-dimensional version of the sigma-coordinate Princeton Ocean Model. The time dependent response of a stratified along-channel flow, forced by barotropic or baroclinic pressure gradients, is examined. Near the bottom, where the along-channel flow is retarded, there is cross-channel Ekman flux that is associated with downwelling on the eastern side and upwelling on the western side of the channel. In the presence of stratification the cross-channel flow rearranges the density structure, which in turn acts on the along-channel velocity via the thermal wind relation. Eventually the cross-isobath Ekman flux is shut down. In the case of baroclinically driven flow of Antarctic Bottom Water through the Vema Channel the model reproduces the observed shape of the deep temperature profiles and their cross-channel asymmetry. The model offers an explanation that is alternative or supplementary to inviscid multilayer hydraulic theory that was proposed in earlier studies. It explains the extremely thick bottom boundary layers in the center and on the western slope of the channel. The deep thermocline is spread out in the west and sharpened in the east, and the coldest water is found on the eastern side of the deep trough. The modified density field reduces the along-channel flow near the bottom and focuses it into a narrow jet on the eastern side of the channel.

1. Introduction

The cold and relatively fresh water formed around the Antarctic continent and modified in the Southern Ocean was called Antarctic Bottom Water (AABW) by *Wüst* [1933]. It is the dominant bottom water mass of the world oceans. *Reid et al.* [1977] further discriminate between three distinguishable water masses that are separated by vertical stability maxima: Weddell Sea Bottom Water (WSBW), Weddell Sea Deep Water (WSDW), and Lower Circumpolar Water (LCPW). Northward spreading AABW forms a deep western boundary current that partly feeds interior gyres [Onken, 1995] but also contributes to a net northward flux that crosses the equator and fills the deep North Atlantic [e.g. *Wright*, 1970]. The Rio Grande Rise at about 30°S separates the Argentine Basin from the Brazil Basin and forms a natural barrier for the bottom waters. Two deep passages, the Vema Channel and the Hunter Channel, and the somewhat shallower Santos Plateau are the pathways through which AABW continues northward. The Vema Channel is the deepest passage, and about 4 Sv (1 Sv = 10^6 m^3 s^{-1}) of the total 6 -7 Sv AABW, estimated by *Speer and Zenk* [1993] to flow from the Argentine Basin into the Brazil Basin, are attributed to this narrow conduit. Moreover, the Vema Channel is the only pathway for the relatively cold WSDW (about 40% of its deep northward transport).

Deep passages, such as the Vema Channel, play a key role in controlling the abyssal circulation, and it is one goal of the Deep Basin Experiment (DBE) of the World Ocean Circulation Experiment (WOCE) to understand how passages affect the flow through them. *Whitehead et al.* [1974] and *Gill* [1977] developed the theoretical framework of rotating hydraulics and show that the volume flux through a strait or passage is limited by the upstream conditions and the geometry of the confinement. Rotating hydraulics have been applied to various oceanic passages and, using sensitive estimates of channel shape and upstream potential vorticity, gave reasonable transport estimates [*Killworth*, 1992; *Whitehead*, 1989]. *Hogg* [1983] used a multilayer hydraulic model and was able to explain several features of the deep flow in the Vema Channel. Observations reported by *Johnson et al.* [1976] and those obtained during the field experiments of the DBE (but also from other passages [*Johnson and Sanford*, 1992]), point to the possible importance of frictional effects. In this study we wish to further elucidate the importance of frictionally induced bottom boundary layer processes and their dynamical implications in an oceanographic setting that resembles the Vema Channel. Another goal of this paper is to test the requirements of numerical resolution to adequately model these processes. Since we wish to concentrate on frictionally induced cross-channel (secondary) circulation, we neglect any along-channel variations in this study. We are aware of the fact that the flow through a constriction is essentially three dimensional and we designed the experiments presented in this paper to be prerequisites for more complicated studies where we shall apply a fully three dimensional modeling approach. The two dimensional geometry, however, allows for a high spatial resolution, simplifies the analysis, and enables us to perform a relatively large number of sensitivity experiments.

The outline of the paper is as follows. In section 2 we review the AABW flow in the Vema Channel and the role of

Paper number 1999JC900055.
0148-0227/99/1999JC900055$09.00

bottom boundary layers on sloping topography. The numerical model is described in section 3, where the numerical experiments are outlined. In section 4 the results of the principle model runs are interpreted. Further sensitivity studies are presented in section 5, and we conclude with a summary in section 6.

2. The AABW Layer in the Vema Channel

The Vema Channel extends about 400 km as a narrow trough oriented approximately north-south (Figure 1). The sill is located at 31°12'S, 39°24'W [*Zenk et al.*, 1993], and the sill depth is somewhat deeper than 4600 m. The main branch of the channel exhibits an asymmetric cross section. The western wall is steep, and the deepest part of the channel is found adjacent to the western side. East of the center, the upward slope is steep but levels out to a broad plateau at about 4200 m. East of the plateau, the topography rapidly shoals again toward the central elevation of the Rio Grande Rise. An apparent feature of hydrographic data from the deep Vema Channel is a cross-channel asymmetry of profiles of temperature and other properties such as light scattering [Johnson et al., 1976]. In the west and near the center there are homogenized, often several hundred meters thick bottom boundary layers and the transition to the overlaying waters is relatively smooth. In the east, where the coldest water is found, the mixed layer is somewhat thinner and capped by a sharp thermocline. Thus the deep thermocline is wedge shaped, being spread out in the west and sharpened in the east, as can be seen from a section from the *Meteor* 15 [*Siedler and Zenk*, 1992] cruise (Figure 2a). One observes that the isotherms generally slope downward to the east, supporting northward bottom water flow bounded by a western wall. In the deepest part of the channel, however, there is a reversal of the isothermal slope and the isotherms converge below the edge of the eastern plateau. Similar structures were also found in the neighboring Hunter Channel [*Speer and Zenk*, 1993] and other passages, such as the Faeroe Bank Channel [*Johnson and Ohlsen*, 1994]. Unfortunately, the western flank of the channel was not well resolved during the *Meteor* 15 cruise. In addition to the isotherms, we therefore include the bottom boundary layer (BBL) heights for individual profiles. These were obtained by determining the height where the temperature had increased by 0.002°C from its bottom value. Several other choices (0.001°C, 0.003°C, 0.004°C, and 0.005°C) were applied. While the first was overly sensitive to slight internal variations within the boundary layer, all higher values gave similar results. Clearly, the thickest bottom layer is located in

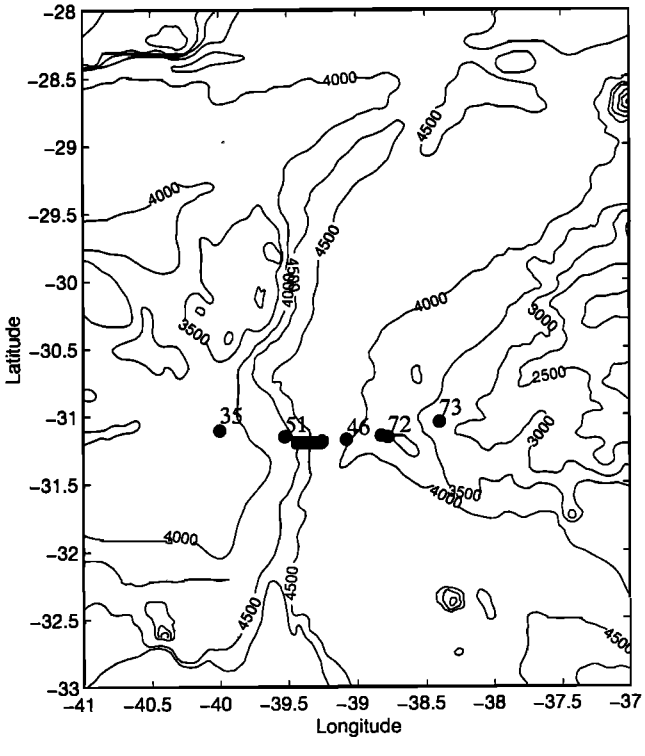

Figure 1. Bottom topography of the Vema Channel and the Rio Grande Rise in the South Atlantic. Isobaths were obtained from the General Bathymetric Chart of the Oceanc (GEBCO) digital atlas. Dots indicate the locations of hydrographic stations from the *Meteor* 15 cruise in 1991.

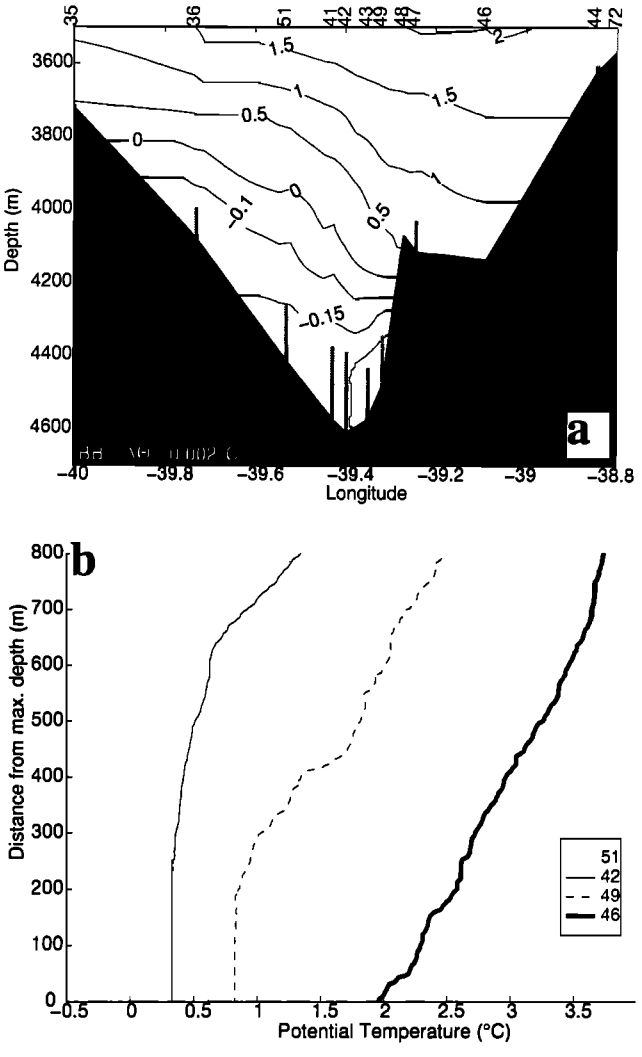

Figure 2. Observed temperature data from the *Meteor* 15 cruise, showing (a) cross section through the Vema Channel at 31.12°S (station numbers indicated on top) and (b) the lowest 800 m of profiles 51, 42, 49, and 46. Temperature offsets are 0.5°C for station 42, 1°C for station 49, and 1.5°C for station 46.

the center of the deep trough, but the homogenized layers at the western slope are well defined and resemble those described by *Johnson et al.* [1976]. Therefore the isotherms that meet the western slope (and were extrapolated nearly horizontally by the contouring program) are more likely to bend downward near the bottom as was indicated in a corresponding section by *Hogg et al.* [1982, Figure 12]. These authors, however, indicated only thin, quasi-isothermal layers at the western slope (but see below). The shapes of individual profiles (Figure 2b) differ considerably over the width of the channel and are consistent with earlier observations [*Johnson et al.*, 1976]. The westernmost profile (station 51) has a nearly homogeneous bottom mixed layer up to about 220 m above the bottom, where there is a transition to a weakly stratified region up to about 450 m. The profile from the center of the channel (station 42) is similar in shape but exhibits an even thicker mixed layer height of about 260 m. The transition to the interior stratification occurs at a height of more than 600 m above the bottom. At the eastern slope of the deep trough (station 49) we observe a distinctively different near-bottom profile. Here the bottom mixed layer is followed by a relatively strong gradient between 200 and 450 m, so that the bottom layer is considerably colder than the overlaying waters. The profile from the eastern terrace exhibits a comparatively thin bottom layer (although it must be stated that there is an uncertainty of a couple of tens of meters about the actual water depth at this particular station), which is capped by a relatively strong gradient at about 40 m. *Sarmiento et al.* [1978] analyzed Geochemical Ocean Section Study (GEOSECS) radon profiles from various oceanic passages. Generally, the standing crop of excess radon 222 was higher in the deep passages than at other nearby locations. In the Vema Channel they found extremely thick bottom mixed layers where radon was spread out several hundred meters above the bottom. Radon has a half-life of a couple of days, so that high concentrations in the water column point to a local emission from the seafloor. *Sarmiento et al.* [1978] concluded that (1) high near-bottom concentration stems from manganese encrustrations that are not covered by sediments owing to rapid near bottom flow and (2) there must be enhanced vertical mixing to distribute the radon concentration over a substantial part of the water column.

Finding the coldest water in the east is a somewhat surprising fact since one expects the deep isotherms to slope downward to the east, supporting a deep northward geostrophic flow in the southern hemisphere. *Hogg* [1983] explained this phenomena using a theory that involves inviscid rotating hydraulics for a multilayer fluid. As a response to accelerating flow in the layers above them, the lowest and coldest layers move eastward and upward to conserve Bernoulli potential and potential vorticity. In particular, the middle layer is spread out in the west and compressed in the east. Potential vorticity conservation requires a velocity maximum in the east where the layer is thin. The decrease of pressure needed to conserve Bernoulli potential is felt by the deeper layer, and the observed homogenization of the deep eastern bottom layer is then a result of extreme vortex stretching forcing isopycnals nearly vertical. The relative vorticity distribution depicted by *Hogg's* [1983] Figure 5.1 accounts for the well mixed layers in the east but not for the homogenized near bottom profiles we found at the western slope. Nevertheless, *Hogg's* [1983] model explained the east-west asymmetry of the temperature section, the vertical stretching of the western part of the middle layer, and the observed recirculation over the eastern plateau.

Johnson et al. (1976), on the other hand, suggested that bottom friction induces a near-bottom cross-channel circulation owing to the Ekman veering of the velocity vector. For a northward flow in the southern hemisphere, this deflection is to the right, looking downstream, thus forcing the coldest water to the eastern side of the channel. Near-bottom current meter data [*Johnson et al.*, 1976; *Hogg et al.*, 1999] show a deviation of the mean velocity vector from the along-channel direction consistent with Ekman veering within a planetary boundary layer. The thick mixed layers were interpreted as a result of enhanced vertical mixing at the location of the near-bottom jet, which was assumed to hug the western channel wall (the latter, however, is inconsistent with *Hogg's* [1983] geostrophic velocity calculations). Laboratory experiments by *Johnson and Ohlsen* [1994], considered to simulate the exchange flow through the Faeroe Bank Channel, corroborated the assumption of considerable frictionally induced secondary circulation in a narrow channel and simulated the observed wedge shape of the deep thermocline.

In recent years the bottom boundary layer for rotating, stratified flow along a slope has received increasing attention (see the review of *Garrett et al.* [1993]). *Weatherly and Martin* [1978] have shown the fundamental asymmetry between downwelling and upwelling modified bottom boundary layers. *MacCready and Rhines* [1991, 1993] have demonstrated that Ekman transport up and down the slope advects heat and salt, altering the local density field. The resulting density gradients reduce the near-bottom along-slope flow and subsequently shut down the cross-isobath flow. The important consequence is that the role of bottom friction in the momentum balance is largely reduced after an adjustment time τ_s. Therefore the authors coined the expression "slippery bottom layers" for the region where isopycnals intersect a sloping bottom and where the along-channel velocity is reduced by baroclinic pressure gradients rather than bottom friction. *MacCready and Rhines'* [1993] theory requires a sloping bottom (slope angle α) and leads to a time-scale of the order of less than a day to years, depending on the bottom slope and stratification

$$\tau_s = \frac{1}{Sf} \tag{1}$$

where $S = (N\alpha/f)^2$ is the slope Burger number. Given a Brunt-Väisälä frequency N typical for the AABW layer of 1.5×10^{-3} s^{-1}, a Coriolis parameter $f = 7 \times 10^{-5}$, and a channel "wall" with an inclination of, say, $\tan \alpha = 2.5 \times 10^{-2}$, we arrive at a shutdown time of 14 hours. According to *Garrett et al.* [1993], (1) must be regarded as an order of magnitude estimate and the shutdown time increases considerably when the diffusive thickening of the boundary layer is taken into account. Most studies on the evolution of bottom boundary layers on a sloping bottom dealt with the case of flow along the continental slope [e.g., *Weatherly and Martin*, 1978; *MacCready and Rhines*, 1993] and considered a region that was unbounded offshore. *Mellor and Wang* [1996], on the other hand, investigated the effect of bottom boundary layer processes on stratified flow within a closed ocean basin. They found that Ekman transports rearranged the density structure over the width of the basin, so that the cross-channel slopes of the isopycnals oppose a surface pressure gradient, leading to reduced abyssal velocities. This process was called "pressure compensation," and *Mellor and Wang* [1996] presented a de-

cay timescale that includes the (flat bottom) basin geometry (depth H and width L),

$$\tau_B = \frac{H}{2C_d|v|}\frac{L^2}{R^2} \tag{2}$$

Here C_d is a drag coefficient, v is the prescribed barotropic velocity, and R is the internal Rossby deformation radius. The timescale τ_B is of the order of 1 year for the oceanic basin considered by *Mellor and Wang* [1996] and about 150 days for the deep trough in the Vema Channel, which has a width somewhat larger than the internal Rossby radius (H = 5000 m, L= 25 km, R=10 km, C_D=3×10^{-3}, v=0.3 m s^{-1}). Thus we expect that the long-term flow through the Vema Channel might be affected by both processes.

In a narrow channel with deep unidirectional flow, downwelling and upwelling occur simultaneously at the respective sidewalls. Water that is downwelled on one side may be trapped in the deepest part of the channel or even be upwelled on the other side. Individual density profiles (Figure 2b) from the Vema Channel are consistent with the picture of bottom mixed layers that are modified by cross slope buoyancy fluxes. In the west, where the flow is downwelling favorable, the BML is thick and "too light" (to use the notation of *DeMadron and Weatherly* [1994]), whereas the profile from the eastern plateau shows a bottom layer that is somewhat thinner, "too dense," and capped by a strong thermocline. In the following we wish to verify the assumption that the flow through the Vema Channel is distinctively modified by frictional effects by applying a two-dimensional numerical model to a cross section of a deep ocean channel.

3. The Numerical Model

The numerical model is a two-dimensional version of the hydrostatic primitive equation Princeton Ocean Model (POM) [*Blumberg and Mellor*, 1987]. The vertical direction is represented by a σ coordinate such that $\sigma = [\eta(x) - z] / D(x)$. D is defined as the total water depth $D(x) = \eta(x) + H(x)$, where H is the water depth and η is sea surface elevation. This bottom-following coordinate system is particularly well suited to the inclusion of bottom boundary layer dynamics. Along-channel (y) gradients are neglected for all prognostic variables, but along-channel gradients of surface elevation η_y and (depth dependent) buoyancy B_y are alternatively prescribed as external forcing terms following *Mellor* [1986]. For simplicity we use a linear equation of state and assume that the density is solely determined by temperature. Thus the governing equations are

$$\frac{\partial \eta}{\partial t} + \frac{\partial (uD)}{\partial x} + \frac{\partial \omega}{\partial \sigma} = 0, \tag{3a}$$

where ω is the vertical (cross sigma) velocity.

$$\frac{\partial (uD)}{\partial t} = -\frac{\partial (u^2 D)}{\partial x} - \frac{\partial (u\omega)}{\partial \sigma} + fvD - gD\frac{\partial \eta}{\partial x} - \frac{gD^2}{\rho_0}\int_\sigma^\eta \left(\frac{\partial \rho'}{\partial x} - \frac{\sigma'}{D}\frac{\partial D}{\partial x}\frac{\partial \rho'}{\partial \sigma}\right) d\sigma' + \frac{\partial}{\partial \sigma}\left(\frac{K_M}{D}\frac{\partial u}{\partial \sigma}\right) + 2\frac{\partial}{\partial x}\left(DA_M\frac{\partial u}{\partial x}\right) \tag{3b}$$

$$\frac{\partial (vD)}{\partial t} = -\frac{\partial (uvD)}{\partial x} - \frac{\partial (v\omega)}{\partial \sigma} - fuD - gD\eta_y - B_y + \frac{\partial}{\partial \sigma}\left(\frac{K_M}{D}\frac{\partial v}{\partial \sigma}\right) + \frac{\partial}{\partial x}\left(DA_M\frac{\partial v}{\partial x}\right) \tag{3c}$$

where $-gD\eta_y$ is a prescribed barotropic pressure gradient and

$$B_y = \frac{gD^2}{\rho_0}\int_\sigma^\eta \frac{\partial \rho'}{\partial y} d\sigma'$$

is a prescribed baroclinic pressure gradient.

$$\frac{\partial (TD)}{\partial t} = -\frac{\partial (TuD)}{\partial x} - \frac{\partial (T\omega)}{\partial \sigma} + \frac{\partial}{\partial \sigma}\left(\frac{K_H}{D}\frac{\partial T}{\partial \sigma}\right) + \frac{\partial}{\partial x}\left(DA_H\frac{\partial T}{\partial x}\right) \tag{4}$$

The boundary conditions at the bottom (σ = -1) are

$$\omega = 0, \tag{5a}$$

$$\frac{K_M}{D}\left(\frac{\partial u}{\partial \sigma}, \frac{\partial v}{\partial \sigma}\right) = \frac{1}{\rho_0}\left(\tau_b^x, \tau_b^y\right), \tag{5b}$$

$$(\tau_b^x, \tau_b^y) = \rho_0 C_D (u_b^2 + v_b^2)^{1/2} (u_b, v_b), \tag{5c}$$

where the drag coefficient is given by

$$C_D = \max[\kappa^2 (\ln(\Delta z_b / z_0))^{-2}, 2.5\times10^{-3}]. \tag{6}$$

Here κ is the von Kármán constant, z_o is the roughness length, and Δz_b is the distance of the deepest velocity grid point from the bottom. The length z_o depends on the local bottom roughness, but in the absence of more specified information a value of 1 cm is used [*Blumberg and Mellor*, 1987]. *Weatherly and Martin* [1978] state that their results showed relatively little sensitivity to the choice of z_o. There is no flux through the bottom and sidewalls, and we do not prescribe any heat flux or wind stress at the surface. The vertical mixing coefficients for velocity and temperature are provided by the embedded turbulence closure model of *Mellor and Yamada* [1982]. The level 2 1/2 version of the submodel requires additional prognostic equations for the turbulence kinetic energy and a turbulence macrolength scale. The full set of equations for the two-dimensional POM model is given by *Allen et al.* [1995]. Horizontal diffusivity and viscosity are defined to act along σ surfaces. In this application we use the two-dimensional version of Smagorinsky's formulation (G. L. Mellor, personal communication, 1996)

$$A_M = C\Delta x^2 [u_x^2 + 0.25 v_x^2]^{1/2}, \; A_H = A_M / Pr. \tag{7}$$

Using high spatial resolution, horizontal diffusion is mainly needed to keep the central difference scheme, used for advection, from producing over- and undershoots. A relative small value of C (0.01) is applied to keep it as small as possible. Typical values of A_M in our calculations are about 5 m^2 s^{-1}. Mean $T(z)$ profiles are subtracted prior to the calculation of diffusion and a Prandtl number Pr = 5 is used to further minimize artificial cross-isopycnal diffusion.

The numerical model employs explicit differencing with leapfrog time stepping together with an implicit scheme for the vertical diffusion terms. A mode-splitting technique is used so that the baroclinic terms can be updated with a larger time step than the barotropic part. For further details of the model the reader is referred to *Blumberg and Mellor* [1987] and *Allen et al.* [1995].

For the two-dimensional experiments we use two realizations of cross-channel sections from an idealized three-dimensional Vema Channel topography. The formulation is based on the function used by *Hogg* [1983], which we also use in upcoming three-dimensional experiments.

$$H(x) = H_0\left[-1 + \tanh\left(\frac{x+1/2\,w}{s}\right) - \tanh\left(\frac{x-1/2w}{s}\right)\right] - 1/2H_P\left[1 - \tanh\left(\frac{x-x_P}{s_P}\right)\right] \quad (8)$$

To approximate the observed bottom form, we use w=120 km, s =30 km, x_P= 10 km, and s_P = 6 km. In the case of the symmetric channel (Figure 3a), H_P is nil and the maximum depth is 5000 m. The asymmetric channel (Figure 3b) has a maximum depth of 4650 m and the plateau levels out at about 4150 m as is roughly the case in the Vema Channel (see Figure 2a). The symmetric bottom profile is depicted together with the sigma surfaces of the numerical grid in Figure 3a. There is a total of 82 sigma levels, and 12 of them are distributed logarithmically near the bottom. Even in the deepest part of the channel, the first 100 m above the bottom are resolved by eight levels. The initial stratification for all experiments is shown with the topography of the asymmetric channel (Figure 3b). The temperature profile approximates mean values from the Vema Channel taken from observations [Speer and Zenk, 1993]. The horizontal grid spacing is 250 m for the basic experiments but was varied for some sensitivity studies. The high-resolution experiments required an external time step of 1.5 s and an internal time step of 45 s. The along-channel pressure gradient (either barotropic or baroclinic) is stipulated externally to the problem. The model is started from rest, and the respective forcing term is ramped up over one inertial period. In the case of a barotropic forcing, which we include because it yields a uniform along-channel velocity in the absence of friction, we prescribe an along-channel pressure gradient $g\eta_y$. The model is spun up until a prescribed total transport (consistent with a uniform along-channel velocity of 0.3 m s^{-1}) is obtained. The forcing is then adjusted to maintain a constant flux throughout the integration time [$(g\eta_y)_t$ is nevertheless small after the initial phase]. Prescribing $g\eta_y$ allows the interior velocities to adjust locally and is therefore preferable to a forcing by an imposed cross-channel elevation gradient. The forcing adjustment mechanism is also necessary to achieve a steady state in those cases where bottom friction is neglected.

The flow of AABW through the Vema Channel is, of course, not barotropic but driven by the density difference between the Argentine Basin and the Brazil Basin. Similar to the forcing of the model by an along-channel elevation gradient, we apply an along-channel baroclinic pressure gradient following *Mellor* [1986]. Typical temperature and salinity profiles from both basins (idealized profiles based on observed data found in the Marine Physics Department's historical database) and the resulting horizontal (pressure dependent) buoyancy gradient $b_y = g\rho_0^{-1}\rho_y$ are shown in Figure 4. Since

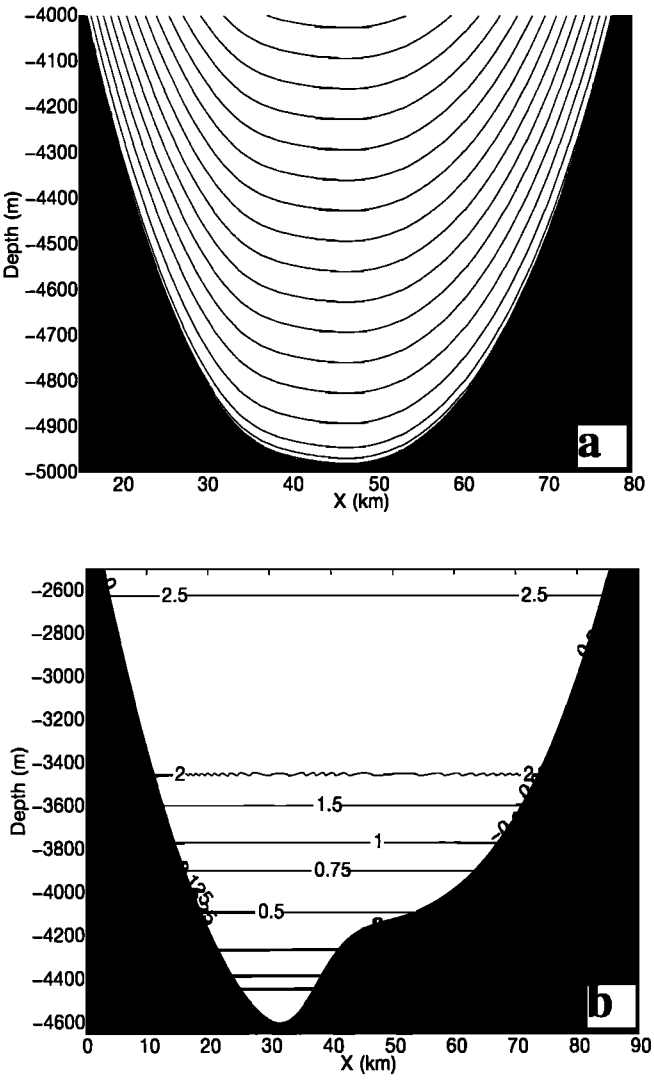

Figure 3. Idealized bottom topographies used in the numerical experiments, showing (a) the symmetric channel together with the σ surfaces of the numerical grid and (b) the asymmetric channel representing the sill region of the Vema Channel together with the initial temperature distribution for all experiments (c_i = -0.15°, 0.0°, 0.25°, 0.5°, 0.75°, 1.0°, 1.5°, 2.0°, and 2.5°C). Orientation is looking into the channel from the south, so that the x-axis increases from west to east.

we are only interested in the deep flow, the profiles were assumed to converge above 2000 m and the buoyancy gradient therefore is nil for the upper part of the water column. The local buoyancy gradient is conveniently approximated by the function

$$b_y(z) = B_0 \exp\left(\frac{(z_{max} - z)^2}{\lambda^2}\right),$$

where B_0 = -9.5 × 10^{-11} s^{-2}, z_{max} = 5000 m, and λ = 1350 m. In the model the buoyancy gradient is evaluated on σ levels. The baroclinic pressure term (see (1c)) requires the vertical integration of the buoyancy gradient

$$B_y = \int_\sigma^\eta b_y\, d\sigma'$$

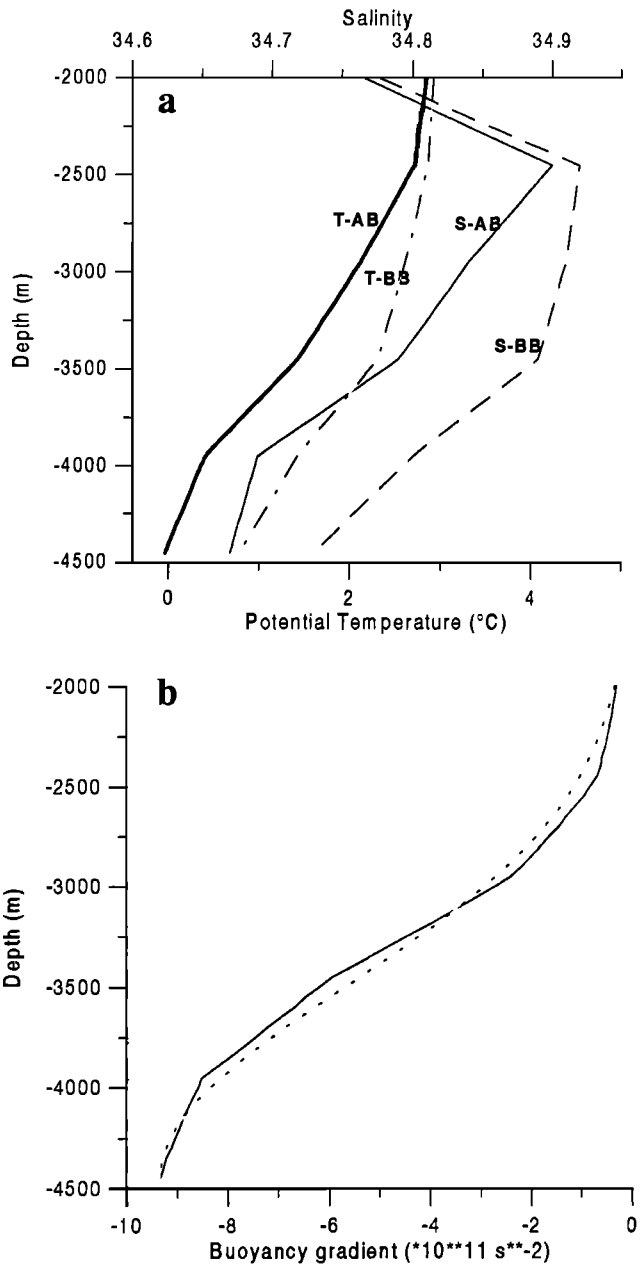

Figure 4. Profiles of (a) temperature T and salinity S from the Brazil Basin (BB) and the Argentine Basin (AB) and (b) the buoyancy gradient based on the density difference between the Brazil Basin and the Argentine Basin (solid line) together with an idealized curve (dashed line).

which is done numerically in the model. Also, in the baroclinic case the forcing is adjusted to maintain a constant northward flux in the deep channel together with the constraint of zero depth-integrated flux (thus there is a southward transport of matching magnitude in the upper layers).

In the following section we present results from our basic experiments. In the first example we use a symmetric channel and the forcing is barotropic. Thus we exclude effects of the asymmetric bottom and the vertical shear of the baroclinic deep flow in the Vema Channel. Deviations from the case without bottom friction are easily detectable, and the physical process is analyzed. Moreover, this allows us to compare the results with those reported by *Mellor and Wang* [1996], who used a similar approach for a wide ocean basin. One difference compared with earlier numerical studies of the bottom boundary layer, such as *MacCready and Rhines* [1993] and *Ezer and Weatherly* [1990], is that these authors prescribed a constant interior velocity as an upper boundary condition for the near-bottom flow, whereas the velocity is allowed to adjust independently here. In the second experiment, baroclinic forcing is imposed and we study the evolution of the flow and density field in the absence of friction. This gives us a reference state for the third experiment, where the Vema Channel is approximated by the asymmetric bottom topography depicted in Figure 3. Experiments 4, 5, and 6 are sensitivity studies discussing the role of the turbulence closure scheme and the numerical grid resolution.

4. Model Results

4.1. Experiment 1: Symmetric Channel, Barotropic Forcing

As a test (not shown), we ran the model without bottom friction (that is, a full-slip condition for the bottommost velocity point was employed). As the forcing is ramped up over one inertial period, the velocities increase linearly and maintain a constant value thereafter. The flow adjusts geostrophically so that in (3b) there is a balance between Coriolis acceleration fv and the barotropic pressure gradient $g\eta_x$ ($\eta_x \cong 30$ cm 100 km^{-1}). Cross-channel velocities are negligible. The effect of horizontal (sidewall) friction is small in these experiments (A_M is proportional to the horizontal velocity shear), and the temperature field remains virtually unchanged. When the model run is repeated with bottom friction, there is considerable cross-channel flow. For a northward along-channel flow on the southern hemisphere, Ekman veering within a planetary boundary layer gives eastward near-bottom flow. This counterclockwise (looking northward in the x-z plane) secondary circulation rearranges the density structure, which, in turn, acts on the along-channel velocity by means of the thermal wind relation (see (3b)). Figure (5a) depicts the temperature section after 180 days of simulations (all fields are averaged over one inertial period). As a result of frictionally induced downwelling and upwelling, the isotherms slope downward near the eastern wall and upward in the west. We observe the fundamental asymmetry between downwelling and upwelling situations that was described by *Weatherly and Martin* [1978] and *Trowbridge and Lentz* [1991]. While upslope transport of relatively cold water stabilizes the water column on the upwelling side, the downslope transport of relatively warm water destabilizes the water column in the bottom mixed layer on the downwelling side, leading to thicker boundary layers there and in the deep trough of the channel. Here the bottom mixed layer is much thicker than the value from the well-known formula $h_M = 0.4u_*/f$, where u_* is the friction velocity. Taking $u_* = 0.013*u_g$, where u_g is the geostrophic velocity in the interior [*Weatherly and Martin*, 1978], this equation yields a bottom mixed layer thickness of only 36 m. At the western slope the near-bottom isotherms are not exactly vertical owing to diffusion at the top of the BBL, and a weak stratification remains within the western BML, consistent with *Garrett's* [1991] finding for a downwelling favorable slope. At the eastern (upwelling) slope the boundary layer becomes thinner as it progresses up the slope owing to suppression of mixing by in-

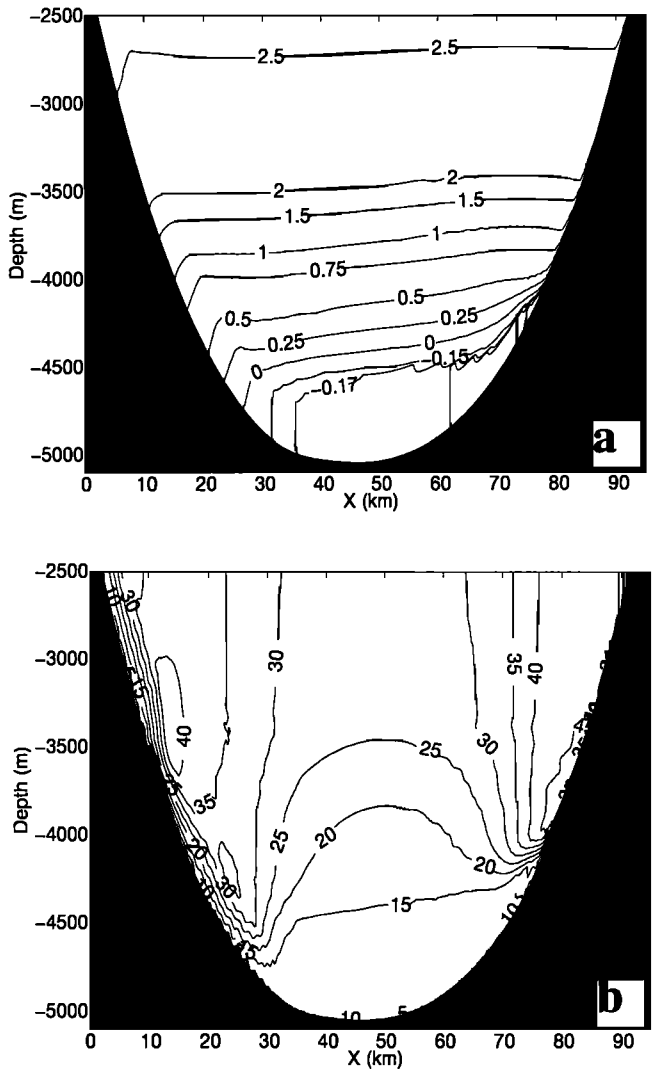

Figure 5. Model results of experiment 1 after 180 days of integration (all fields are averaged over one inertial period), showing (a) temperature (c_i = -0.023°, -0.021°, -0.019°, -0.017°, -0.015°, 0, 0.25°, 0.5°, 0.75°, 1°, 1.5°, 2°, and 2.5°C) and (b) along-channel velocity (c_i= 5 cm s^{-1}).

creased density contrast and restratification. The temperature BMLs are therefore capped by a strong thermocline in the east. In addition to the strong tilt of the isotherms directly near the sloping bottom, the isotherms slope upward to the right over the width of the channel, resembling the results of *Mellor and Wang* [1996] for a much wider basin. The along-channel velocities (Figure 5b) are reduced near the bottom but also in the interior over the center of the channel. The near-bottom region of high velocity shear is much thicker in the west and corresponds to the temperature BML there. In the center the velocities are reduced owing to the baroclinic pressure gradient induced by the general upward slope to the east of the isotherms. Although the temperature is homogenized over a couple of hundred meters, the thickness of the near-bottom velocity shear layer is only a few tens of meters.

In Figure 6 we depict the cross-channel (see (3b)) and along-channel (see (3c)) momentum balances for the near-bottom flow (taken along σ level 78). The terms of (3b) and (3c) were evaluated after 180 days of integration and averaged over one inertial period. In the cross-channel part (Figure 6a) the barotropic pressure gradient is largely balanced by the baroclinic pressure gradient owing to cross-channel density variations. This effect is most pronounced on the steep flanks of the channel. This is the balance predicted by *MacCready and Rhines* [1993] in their theory of the "shutdown" of the Ekman flux by buoyancy forces. Even in the center of the channel, the baroclinic pressure gradient is much stronger than the Coriolis acceleration. The baroclinic buoyancy gradient near the bottom is not only determined by the horizontal density variations in the deep trough but also feels the slope of the isotherms higher in the water column. This is the effect of "pressure compensation" discussed by *Mellor and Wang*

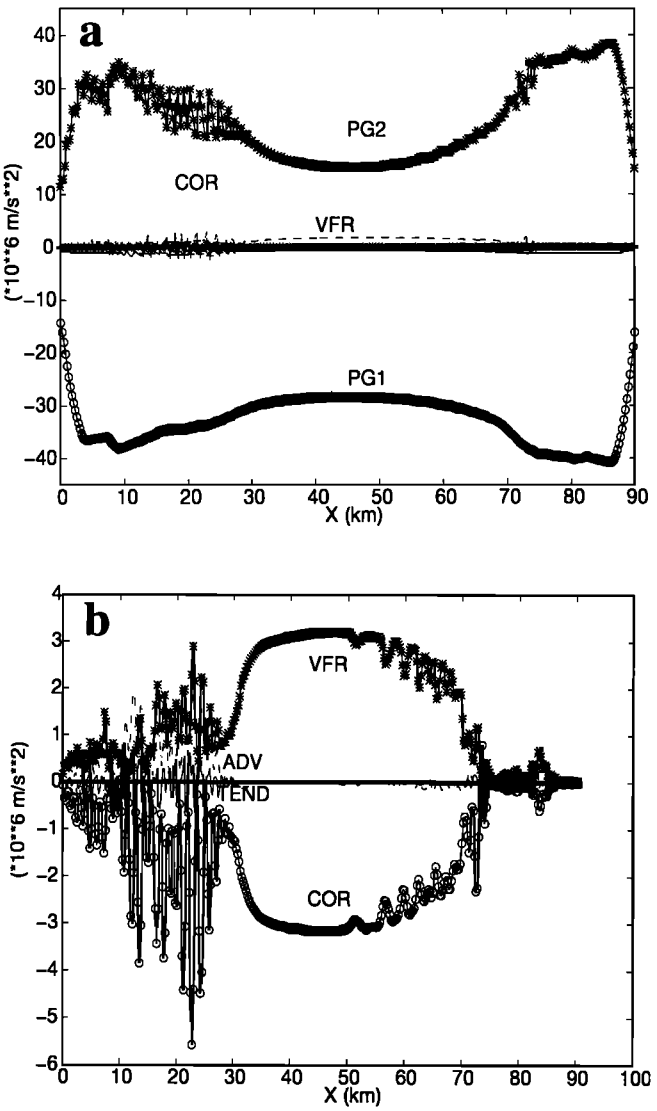

Figure 6. (a) Cross-channel (x) momentum balance of the near-bottom (σ level 78) flow in experiment 1 after 180 days of integration and averaging over one inertial period; COR = $-fvD/H$, VFR = $\partial/\partial_z(K_M\,\partial/\partial_z u)$, PG1 = $g/H\partial/\partial_x\eta$, PG2 = $gD^2/(H\rho_0)\int[\,\partial/\partial_x\rho - \sigma/D(\partial/\partial_x D\;\partial/\partial_\sigma\rho)]\partial\sigma$.
(b) Same as Figure 6a but for along-channel (y) momentum balance; COR = fuD/H, VFR = $\partial/\partial_z(K_M\,\partial/\partial_z v)$, TEND = $1/H[\partial/\partial_t(vD)]$, ADV = $1/H[\partial/\partial_x(uvD) + \partial/\partial_\sigma(v\omega)]$.

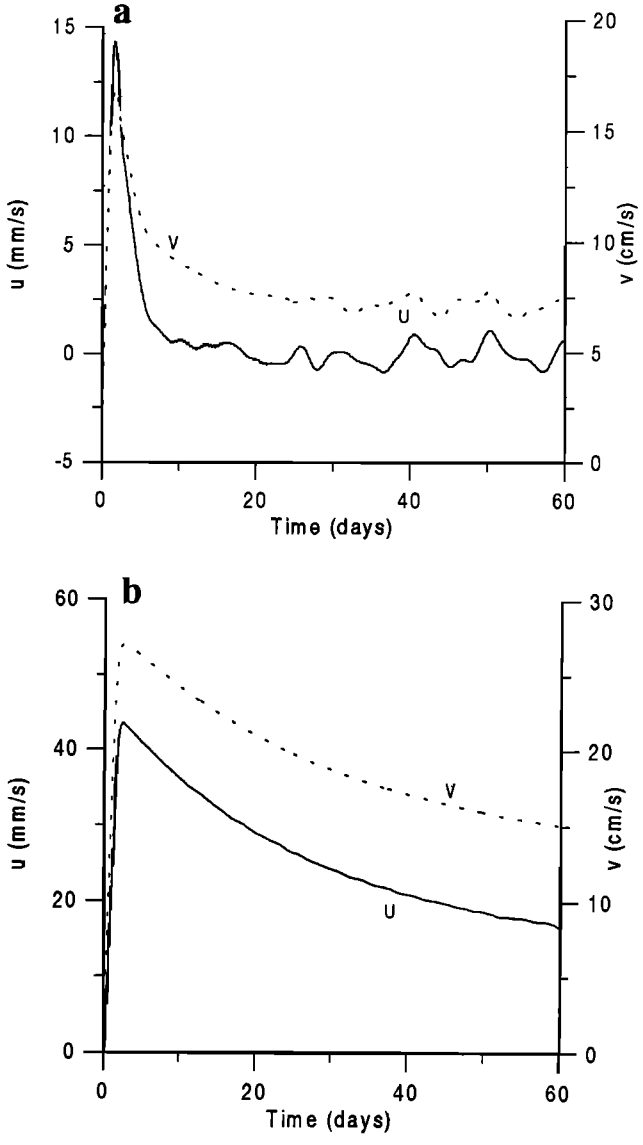

Figure 7. Time series of the near-bottom flow (note the different scaling of the cross-channel velocity u and the along-channel velocity v for the first 60 days of experiment 1 taken (a) at a location at the eastern slope (x = 75 km) and (b) at the center of the channel (x = 45 km). All time series are filtered to suppress inertial variations.

[1996]. It is important to note that the baroclinic and the barotropic pressure gradients together nearly balance the Coriolis acceleration, making the geostrophic assumption valid over most parts of the channel. In Figure 6b the along-channel momentum balance for the near-bottom flow is displayed. There are three different dynamical regimes. A linear Ekman balance between Coriolis term and vertical friction holds only in the central region of the channel. The velocity boundary layer is essentially a neutral layer, and its thickness is well expressed by the $h_M = 0.4u_*/f$ limit. On the upwelling side the cross-slope transport is almost shut down and both terms are small with some disturbances. On the downwelling side of the channel we observe that the tendency and the advection term play a considerable role in the balance. Here warm water is advectively downwelled under colder water, destabilizing the water column and inducing convective motion.

The different adjustment timescales for the slopes and the flat bottom region can be seen by comparing time series of cross-channel velocities from a location near the center (Figure 7a) and from a location on the eastern side of the channel where the slope is steepest (Figure 7b). In the latter the upslope velocity almost ceases completely after a time of about 2 days after the initial spin-up, whereas there is a much slower decay in the center. Figure 8a depicts a respective time series from the western channel wall (x = 25 km). The initial decay of the cross-channel velocity is similar to the upwelling side. Immediately after the cross-channel velocity is spun down considerably, however, it starts to oscillate with a period of roughly 2 days. The amplitude is about 4 mm s^{-1} superim-

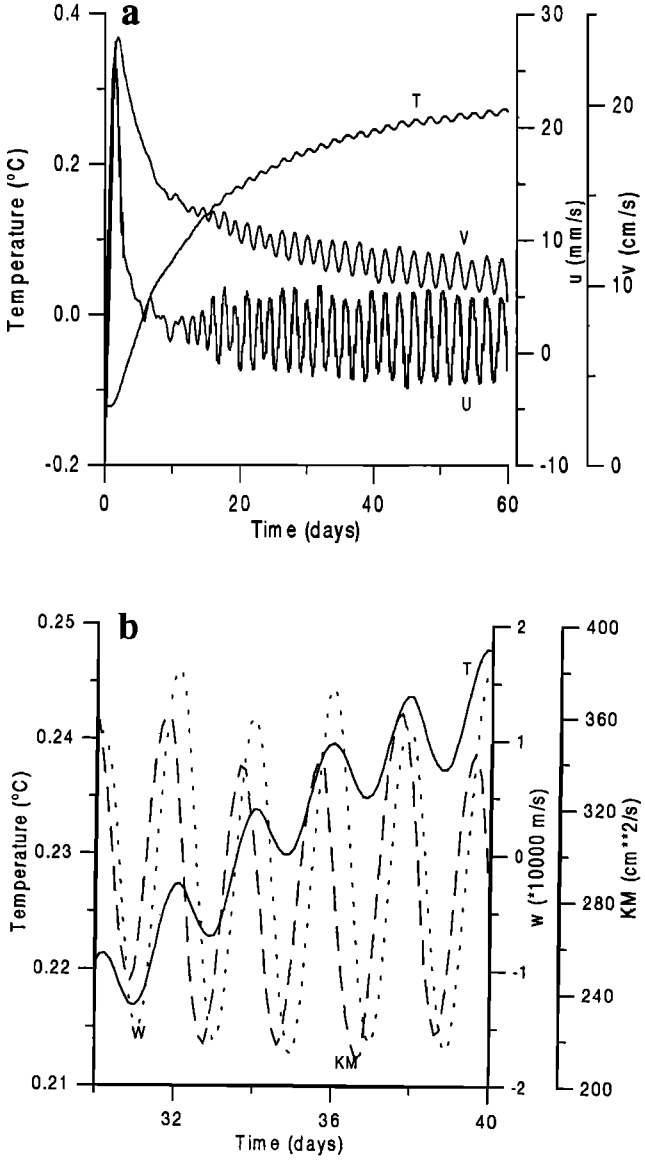

Figure 8. Time series from a location at the western slope of the channel (x = 25 km), showing (a) the evolution of the near-bottom flow (cross-channel velocity u, along-channel velocity v and temperature T during the first 60 days of experiment 1 and (b) temperature, vertical velocity w and vertical friction coefficient K_M during a 10-day period.

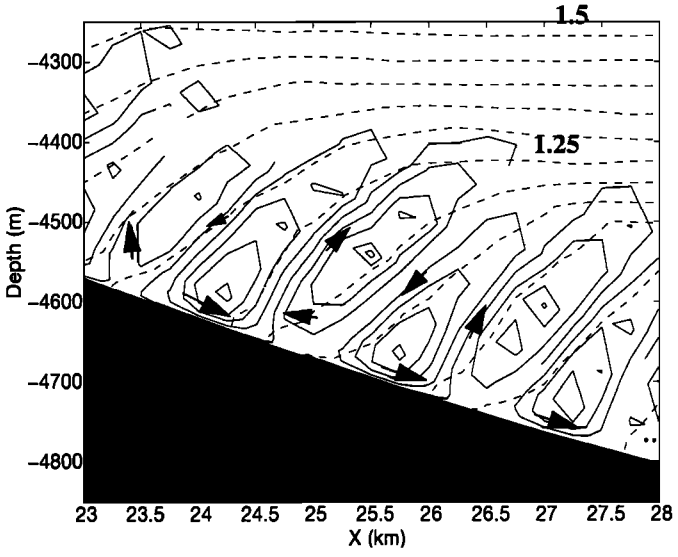

Figure 9. Cross-channel stream function ψ (solid lines, c_i = 0.1 m^2 s^{-1}) and temperature (dashed lines, c_i = 0.05°C) from experiment 1 after 180 days of integration for a limited domain at the western slope of the channel.

posed onto a mean value of about 2 mm s^{-1}. Note that these oscillations are different from the inertial oscillations predicted by *Weatherly and Martin* [1978] and reproduced by *MacCready and Rhines* [1993], which have a period $T = 2\pi/(f(1+S)^{1/2}) \leq 2\pi/f$. The time dependency is seen in all variables, and the positive warming trend due to the downward slumping of warmer water has a small periodic variation superimposed. Figure 8b shows a blowup of the temperature time series together with the respective ones for vertical velocity ω (the cross-σ velocity) and the vertical friction coefficient K_M. Within the turbulent bottom layer, K_M is generally high with a mean value of 300 cm^2 s^{-1} (whereas it is generally an order of magnitude smaller at the eastern side). When there is enhanced downslope flow, the near-bottom temperature rises and reduces the stability, so that the turbulent mixing coefficient increases. These events are also linked to relatively strong vertical velocities (up to 15 m day^{-1}), indicating a convective process. The oscillations were a persistent feature in the experiment and did not decay even for long integration times (up to 900 days). To evaluate the cross-channel (x-z plane) circulation, we calculate a stream function Ψ,

$$\psi(x,\sigma)=\int_{-1}^{\sigma} u(x,\sigma)\,d\sigma'$$

The Ekman induced, near-bottom, cross-channel flow is generally counterclockwise (i.e., eastward) near the bottom, but the downwelling side of the channel exhibits relatively large, organized recirculation cells. Figure 9 shows these cells for a limited domain at the deep western flank of the channel. The vertical extent of the cells is of the order of the BML, and they are aligned to the isotherms. The cells are about 1-1.5 km wide at the western slope (thus they are resolved by at least four numerical grid cells); they are smaller and only marginally resolved in the deepest part of the channel and do not exist in the east. We used different horizontal resolutions to make sure that their size did not depend on the numerical grid. The time series (Figure 8a) indicate that the oscillations start after the initial shutdown is almost completed, and an analysis of the term balance in the temperature equation (4) from this particular region (not reproduced here) showed a dominant balance between temporal variations $(DT)_t$ and advection by the velocity field $[(uTD)_x + (\omega T)_\sigma]$. The cells are a consequence, not the cause of the thick mixed layers in the west, and temperature is largely conserved on fluid particles as they are advected. Nevertheless, Figure 9 shows that the cells slightly modify the temperature field. For example, at x = 25.25 km and z = -4500 m the 1.25°C isotherm is uplifted relative to the one just underneath. At the bottom these isotherms converge owing to opposing near-bottom flow. A vertical profile of this (overall weakly stratified) part of the water column would therefore show a slightly more homogenized region, where isotherms diverge followed by enhanced stratification near the bottom. This could possibly explain internal variations of the vertical temperature gradient within the bottom boundary layers, which were found west of the Vema Channel axis by *Johnson et al.* [1976].

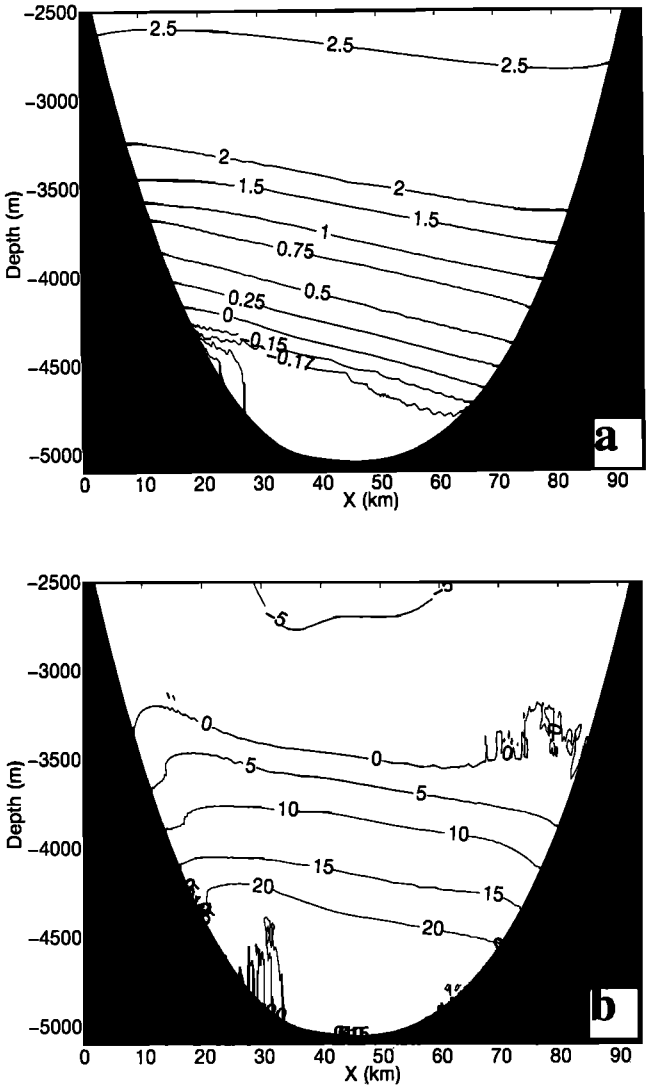

Figure 10. Model results of experiment 2 after 180 days of integration, showing (a) temperature (c_i = -0.021°, -0.019°, -0.017°, -0.015°, 0°, 0.25°, 0.5°, 0.75°, 1°, 1.5°, 2°, and 2.5°C) and (b) along-channel velocity (c_i= 5 cm s^{-1}).

The recirculation cells bear striking similarity to those found by *Allen and Newberger* [1996] in their numerical simulations of the downwelling circulation on the Oregon continental shelf. They describe periodic separation and reattachment of the bottom boundary layer and accompanying closed circulation cells. The authors attribute these cells to a symmetric (slantwise) instability as a result of a combination of the mechanisms responsible for inertial instability in a rotating nonstratified flow and for convective instability in a stratified nonrotating flow. When warmer water is downwelled under higher-density fluid, symmetric instability can develop before the flow becomes convectively unstable. Also, *Ezer and Weatherly* [1990], in their simulations of a cold filament on a sloping bottom, found enhanced vertical circulation and closed circulation cells in locations where the water column was destabilized statically. *Allen and Newberger* [1996] found that the width of the cells scale with the along-slope velocity, consistent with what we find in our experiments. However, an aspect ratio γ of $O(0.1)$ and a u/ω ratio of a similar magnitude raise the question if this process might be nonhydrostatic. Moreover, the circulation cells are found within the mixed layer where N^2 is small. *Marshall et al.* [1997] introduced the criterion $n=\gamma^2/Ri^2 << 1$, where Ri is the Richardson number, for the hydrostatic assumption to be valid. In our experiments, Ri is small, at least locally in the BML, so that this requirement is certainly not met. *Marshall et al.* [1997] conducted numerical experiments comparing a nonhydrostatic model with a hydrostatic model. For the case of near-surface convection they found that the hydrostatic model reproduced the convective overturning, even though the vertical acceleration term was absent. The hydrostatic model, however, overestimated the overturning velocity and the resulting baroclinic structure was less coherent than in the nonhydrostatic experiments. On the basis of a number of sensitivity studies with different horizontal and vertical resolution, we conclude that downwelling-induced symmetric instability is a realistic feature in downwelling favorable regions over sloping topography and especially within a narrow channel where the downwelled water is trapped in the deep trough. The vertical circulation plays an important role in the observed detachment of bottom boundary layers [*Armi and D' Asaro*, 1980; *Ezer and Weatherly*, 1990] and for the distribution of tracers such as radon over a substantial part of the water column as observed by *Sarmiento et al.* [1978]. More research is necessary, however, to further explore the nonhydrostatic nature of the unusual phenomenon of upward convection in the ocean.

4.2. Experiment 2: Symmetric Channel, Baroclinic Forcing, No Bottom Friction

As a starting point for the more realistic experiments with baroclinic forcing, we demonstrate the spin-up of the model when there is no bottom friction. The depth-dependent, along-channel flow adjusts geostrophically via the thermal wind relation. The isotherms are uplifted in the west and sink in the east, thus bringing the coldest water to the deep western side of the channel (Figure 10a). The flow is in thermal wind balance, and so the along-channel velocities increase with depth below the 2° isotherm. The highest velocities are found together with the core of the cold bottom water (Figure 10b). The slope of the 1°C and 1.5°C isotherms is close to the observations from the Vema Channel, and the along-channel velocities change sign near the 2° isotherm, which is often used as a level of no motion in geostrophic calculations. The initial adjustment requires negative (westward) cross-channel velocities in the beginning that vanish after an adjustment time of about 30 days (Figure 11). Rerunning the experiment using the asymmetric bathymetry displayed in Figure 2b gave qualitatively similar results, which are therefore not shown here.

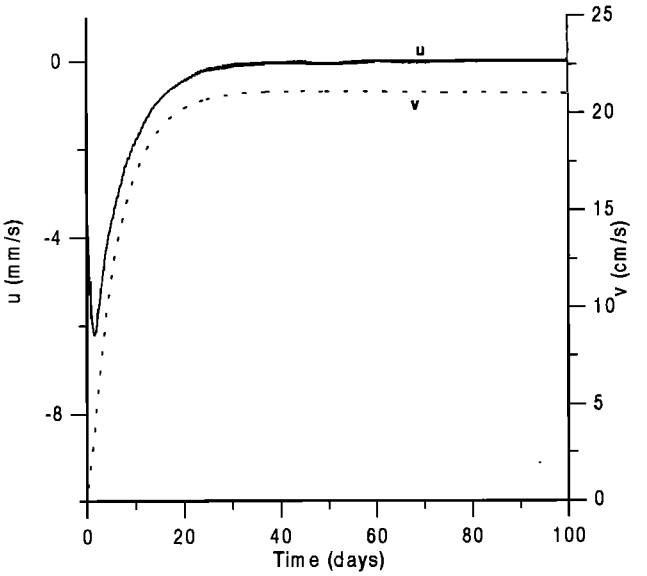

Figure 11. Time series of cross-channel velocity u (solid line) and along-channel velocity v (dashed line) from a location at the western slope of the channel (x = 25 km) for the first 100 days of experiment 2.

4.3. Experiment 3: Asymmetric Channel, Baroclinic Forcing, Bottom Friction

Finally, we describe an experiment with bottom friction and the asymmetric topography that represents the bottom structure of the sill region of the Vema Channel. Here the forcing is, as in experiment 2, baroclinic, and this experiment is the one considered to be most realistic, although we cannot expect to exactly reproduce the observations, given the idealizations applied. The model was run for 900 days, and results are displayed after 360 days and averaging the variables over one inertial period. Figure 12 shows a time series from a location west of the channel axis (x = 25 km). During the first couple of days the spin-up is similar to the frictionless case shown in Figure 11. The along-channel flow v adjusts geostrophically. The cross-channel velocity u is initially westward to install the isothermal slope required for northward flow. As v increases downslope, Ekman flux sets in, changing the sign of u. The along-channel velocity v reaches a maximum at about 20 days and decreases thereafter as does the cross slope velocity. The decay time is considerably longer here compared with experiment 1 and equation (1). The reason is probably that N^2 is permanently reduced during the adjustment phase on the downwelling favorable side (Figure 13a). At the respective slopes we observe upwelling and downwelling. Thick BMLs are found at the deep western wall and in the center. Since the Ekman-induced, cross-channel velocity depends on the magnitude of the along-channel velocity, there is only weak downwelling in the those parts of the water column where v is small (Figure 13b). Therefore the thickness of the homogenized lay-

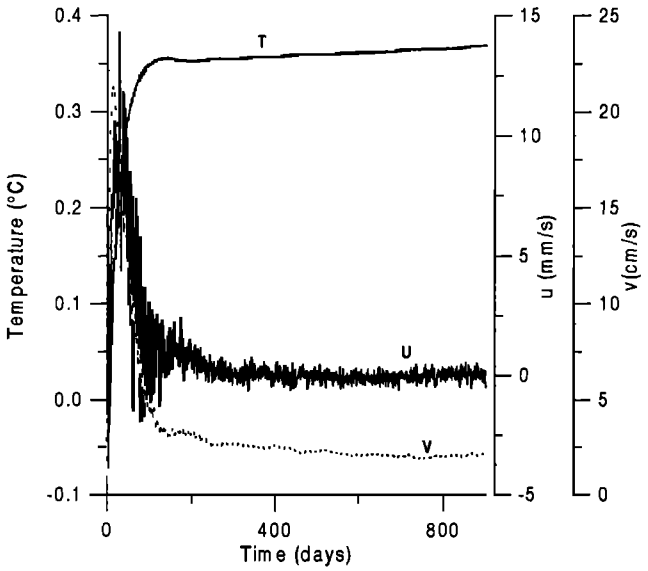

Figure 12. Time series of cross-channel velocity u, along-channel velocity v and temperature T from a location at the western slope of the channel (x = 25 km) during the run time of experiment 3.

ers at the western slope decreases upslope. As a result of this localized downwelling in the lower part of the western side, the thermocline spreads out over several hundred meters. The opposite is true for the deep eastern slope; the isotherms tend to slope downward to adjust geostrophically to the northward flow, but there is opposing upslope transport of relatively cold water near the bottom. There is a convergence of the isotherms near the edge of the plateau. The 0.25°C isotherm slopes upward to the east over the width of the deep trough, indicating pressure compensation. The temperature field suggests that the reduction of the baroclinic pressure gradient $(\rho_0^{-1} g \rho_x)$ is most pronounced on the western side, so that along-channel velocities also decrease via the thermal wind relation (see equation (3b)). Thus the highest along-channel velocities are found within the deep trough but the maximum has moved to the eastern side of the channel. Another way of looking at this is that the isothermal separation, say, for example, between the 0.5° and the 0.25°C isotherm, decreases dramatically toward the east. Potential vorticity conservation then requires positive relative vorticity v_x, bringing the maximum close to the eastern plateau where the relative vorticity must change sign owing to sidewall friction there.

Figure 13c depicts the difference between the along-channel velocity (Figure 13b) and the model-calculated geostrophic velocity from evaluating the equation

$$v_g = \frac{g}{f}\frac{\partial \eta}{\partial x} + \frac{gD}{f\rho_0}\int_{\sigma}^{\eta}\left(\frac{\partial \rho'}{\partial x} - \frac{\sigma'}{D}\frac{\partial D}{\partial x}\frac{\partial \rho'}{\partial \sigma}\right) d\sigma' \ .$$

The flow is in geostrophic equilibrium, save for those parts of the channel where, as in experiment 1, organized recirculation cells occur. Even there, however, the ageostrophic part accounts for no more than about 10% of the total along-channel velocity. Thus, even though the specific shape of the density field is caused by ageostrophic frictional effects, the accuracy of geostrophic calculations from observed temperature and sa-

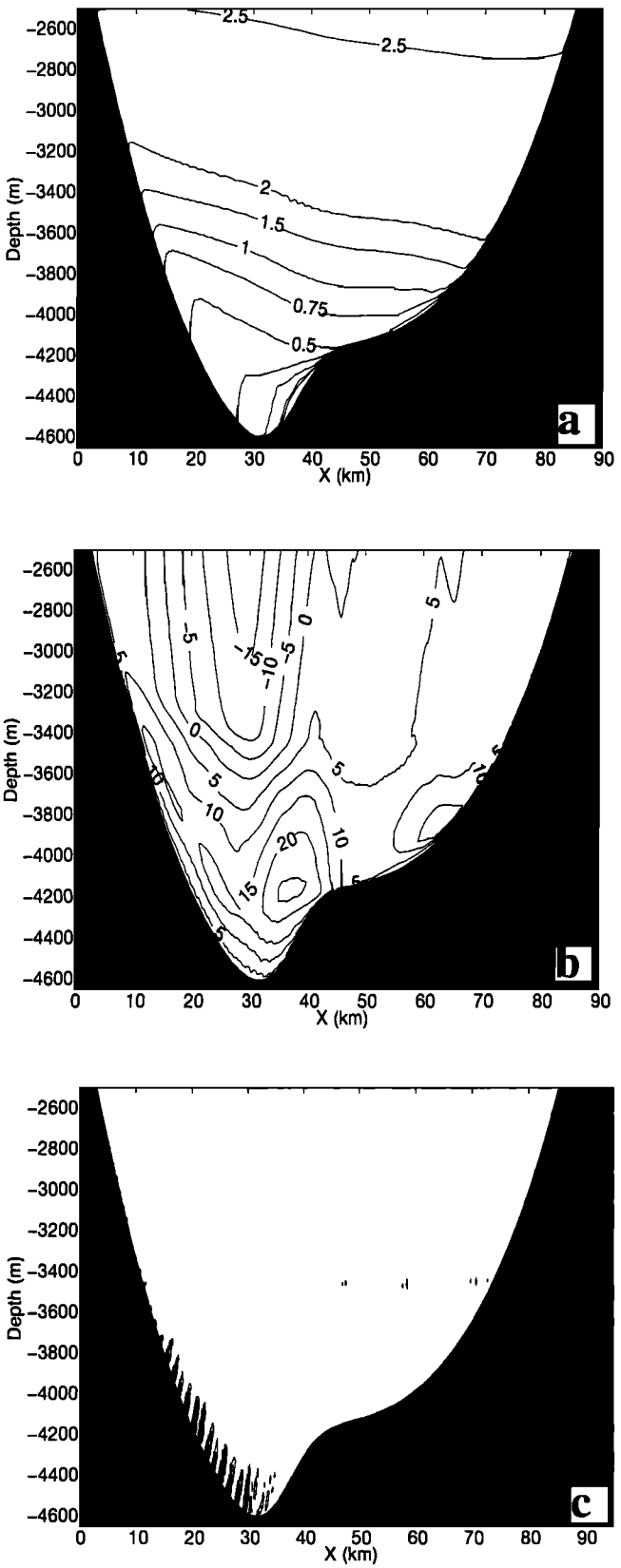

Figure 13. Model results of experiment 3 after 360 days of integration, showing (a) temperature (c_i = -0.017°, -0.015°, 0°, 0.25°, 0.5°, 0.75°, 1°, 1.5°, 2°, and 2.5°C), (b) along-channel velocity (c_i= 5 cm s^{-1}), and (c) the difference $|v - v_g|$ between the along-channel velocity and the model-calculated geostrophic velocity (c_i = 0.1 mm s^{-1}).

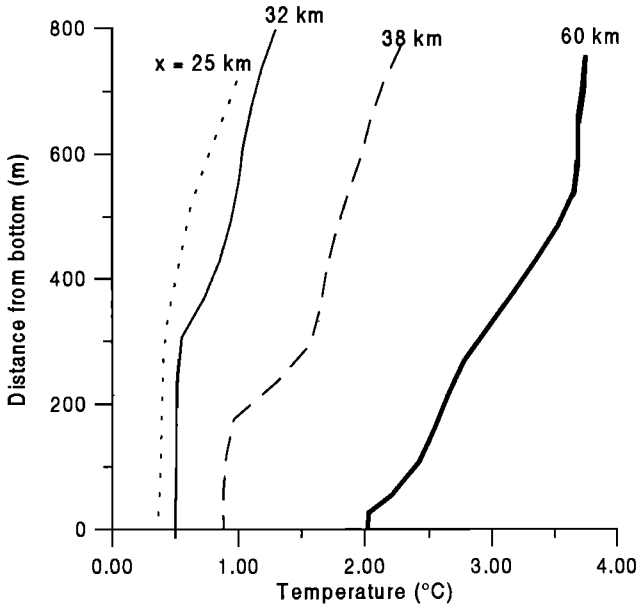

Figure 14. Model-calculated (experiment 3) temperature profiles for the lowest 800 m above the bottom from various locations (resembling those from Figure 2b) across the channel. Temperature offset is 0°, 0.5°, 1°, and 1.5°C from left to right.

linity fields will not be seriously influenced (compared to other sources of errors, such as the determination of the layer of no motion). The recirculation cells are similar to those found in experiment 1 and are not reproduced here. One discrepancy between the modeled velocity field and the observations is that the latter report southward flow over the eastern plateau [*Hogg et al.*, 1982; *Johnson*, 1984; *Hogg et al.*, 1998]. The southward flow was explained by *Hogg* [1983] as a result of the stretching of the upper layer in the east requiring negative relative vorticity.

Profiles of model temperature (Figure 14) reproduce the observed shape and cross-channel asymmetry (Figure 2b). In the west of the channel there is a smooth transition above the bottom layer, and a weak stratification remains in the near-bottom layer as is typical for a downwelling-modified bottom mixed layer. This is probably the explanation for the relatively thin isothermal regions (in which the vertical temperature change was less than 0.001°C) on the western side of the Vema Channel reported by *Hogg et al.* [1982]. Their criterion disregarded weakly stratified regions, although they are obviously homogenized compared to the ambient stratification. In the center of the channel the mixed layer is more than 300 m high, followed by a transition zone with increased temperature gradient. Going farther to the east and up the slope of the narrow trough, the profile at x = 38 km exhibits a "to cold" anomaly over the thickness of the bottom layer, typical for an upwelling modified BBL. A profile from the eastern plateau indicates upwelling as well but, owing to the moderately sloping bottom and the relatively weak along-slope velocity, the bottom mixed layer is only about 30 m thick.

5. Sensitivity Studies

5.1. Experiment 4: Constant Vertical Friction Coefficients

Experiment 3 was rerun, but the vertical friction coefficients K_M and K_H were set to a constant value of 5×10^{-4} m^2 s^{-1}. Figure 15 shows the temperature section after 180 days of integration. Comparing the temperature field with Figure 13, we see that the general baroclinic structure is reproduced. There are the thick bottom boundary layers on the western side and in the center of the channel. The temperature field looks generally smoother than in the case with the *Mellor and Yamada* [1982] scheme. The boundary layer heights are lower on the downwelling favorable side, and there is only weak upwelling east of the plateau. Generally, the discrepancies are more pronounced on the eastern, upwelling favorable side of the channel. This is consistent with a recent numerical study of *Middleton and Ramsden* [1996], who found that the assumption of a constant Richardson number (and related vertical friction coefficient) is problematic, especially for the upwelling favorable case. The recirculation cells at the western channel wall were also present in this experiment, corroborating *Allen and Newberger*'s [1996] finding that inviscid dynamics are strongly involved in their evolution.

5. 2. Experiments 5 and 6: Role of Numerical Grid Resolution

The high resolution we used in the basic experiments was basically needed to resolve the small-scale features such as the recirculation cells at the downwelling favorable channel wall. However, as pointed out earlier, this study was designed as a prerequisite for three-dimensional model studies, where we cannot, of course, maintain a horizontal resolution of 250 m. Therefore we conducted some sensitivity experiments regarding the numerical grid. In experiment 5 the horizontal grid spacing is 5000 m, and in the vertical there are 32 σ levels, 9 of them in a logarithmic boundary layer near the bottom. This is about the maximum we are able to achieve in a regional model focusing on the Vema Channel. Figure 16 a depicts the temperature field after 360 days. Although there is more upwelling on the eastern side and the isotherms converge over the plateau, rather near the edge of the plateau, the basic isothermal structure of experiment 3 is still reproduced. There are

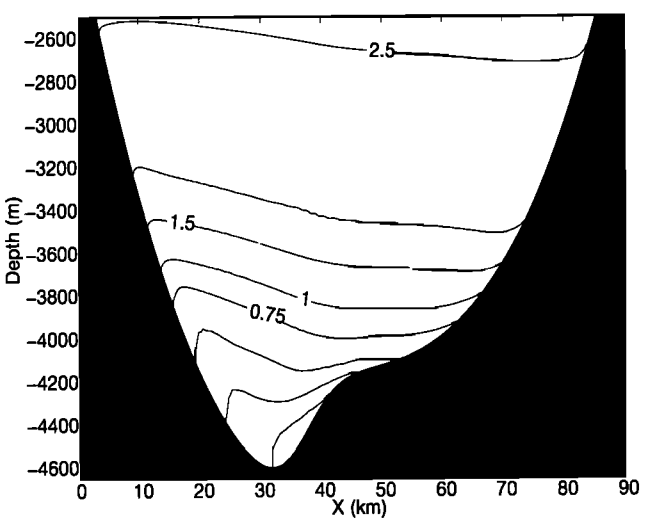

Figure 15. Model results of experiment 4 ($K_M = K_H = 5 \times 10^{-4}$ m^2 s^{-1}) after 360 days of integration, showing (a) temperature (c_i = 0°, 0.25°, 0.5°, 0.75°, 1°, 1.5°, 2°, and 2.5°C) and (b) along-channel velocity (c_i= 5 cm s^{-1}).

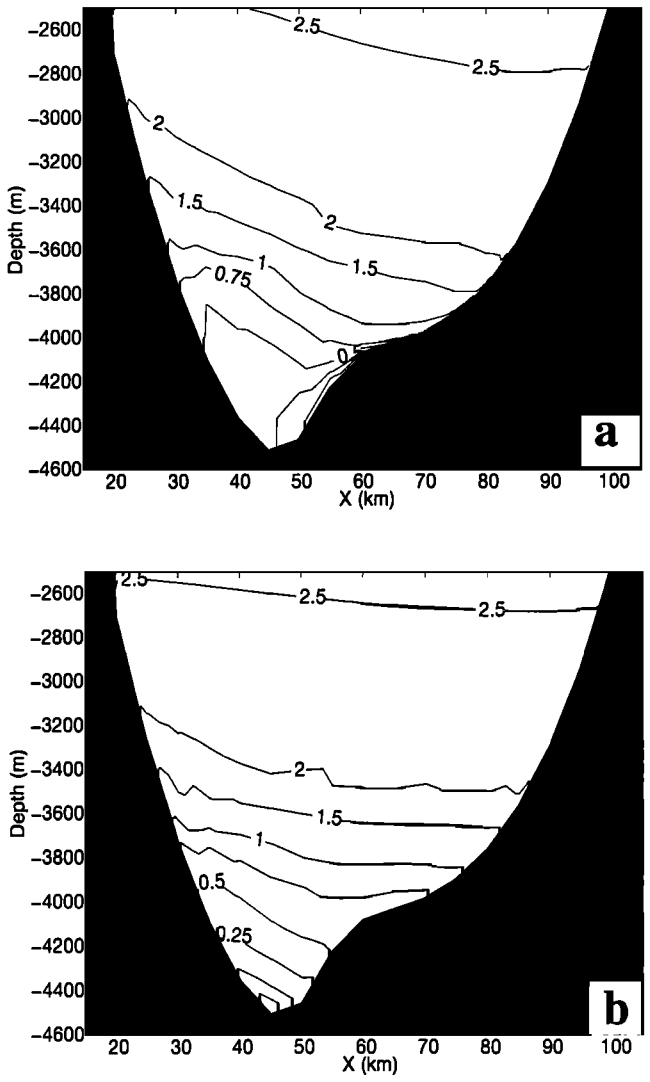

Figure 16. Comparison between two coarse resolution model runs. Temperature fields were obtained from model runs with (a) enhanced vertical resolution near the bottom (experiment 5) and (b) without the logarithmical σ level distribution near the bottom (experiment 6).

thick mixed layers near the bottom, and there is the observed reversal of the slope of the isotherms. In experiment 6 the same model configuration was used but without enhanced vertical resolution near the bottom (Figure 16b). At a water depth of, say, 4500 m the vertical resolution is about 140 m throughout the water column. In this case the bottom boundary layer was not well enough resolved. The modification of the temperature field is too weak to introduce a reverse of the isothermal slope at depths, and the overall distribution of temperature and velocity resembles more the case that was run without bottom friction. From these experiments we conclude that the bottom boundary layer can be adequately resolved, even in deep water by a moderate number of total levels, when a sigma distribution with enhanced resolution near the bottom is chosen.

6. Summary

A two-dimensional model study on the frictionally modified flow through a deep channel is presented. The basic dynamical features are explained for the simplified case of barotropically driven, along-channel flow through a symmetric channel. Frictionally induced anomalies are identified by comparing the results with the inviscid case where isotherms remain flat and no cross-channel transport evolves. It is shown that the modification of the near-bottom temperature field is part of an adjustment process that was earlier described by *MacCready and Rhines* [1991, 1993], for the case of constant slope angle, using analytical and one-dimensional numerical models. The cross-channel slope of the isotherms within the narrow trough is modified over the width of the channel by upwelling and downwelling, leading to pressure compensation [*Mellor and Wang*, 1996].

The more realistic case of a deep flow driven by a large-scale baroclinic pressure gradient through an asymmetric channel reproduced several observed features of the flow and temperature fields in the Vema Channel. This is particularly true for the thick, downwelling-modified, bottom boundary layers found on the western side of the channel, which could not be explained by hydraulic theory. The modeled temperature section shows qualitative agreement with the observed field. There are the wedge-shaped, deep thermocline and the thick BMLs in the deep channel. The former was explained by *Hogg* [1983] using inviscid hydraulic theory. Geostrophic velocity calculations by the same author suggested that the along-channel velocities are strongest at the eastern side, where the isotherms converge, again in agreement with rotating hydraulic theory. Our results show, however, that the frictionally induced rearrangement of the density structure can also account for the focusing of the along-channel flow into a narrow jet located approximately at the edge of the deep plateau. Although both the mechanism presented here and rotating hydraulics are considerably different, their effect on the deep thermocline and the baroclinic velocity distribution are quite similar in terms of potential vorticity conservation. The compression of the isotherms at the edge of the plateau and the vortex stretching in the west require relative vorticity to increase toward the east, leading to a maximum of along-channel velocity there. This study is not challenging the validity of *Hogg*'s [1983] multilayer rotating hydraulic model. Rather, hydraulic and frictional effects are expected to overlap, in reality. The along-channel flow, which is influenced by hydraulic processes such as uplifting and separation, will be subject to the frictional effects discussed here. In an upcoming three-dimensional study we therefore wish to examine the relative role of bottom friction and hydraulic control in the modification of bottom water flow through the Vema Channel.

Acknowledgments. This work was funded by the German Ministry of Science and Technology (BMBF, WOCE II-IV). Helpful comments of N. Hogg and an anonymous reviewer are gratefully acknowledged.

References

Allen, J. S., P. A. Newberger, and J. Federiuk, Upwelling circulation on the Oregon Continental Shelf,I, Response to idealized forcing, *J. Phys. Oceanogr.*, *25*, 1843-1866, 1995.

Allen, J. S., and P. A. Newberger, Downwelling circulation on the Oregon Continental Shelf, I, Response to idealized forcing, *J. Phys. Oceanogr.*, *26*, 2011-2035, 1996.

Armi, L., and E. D'Asaro, Flow structures of the benthic ocean, *J. Geophys. Res.*, *85*, 469-484, 1980.

Blumberg, A. F., and G. L. Mellor, A description of a three-dimensional coastal ocean circulation model, *Three-Dimensional Coastal Ocean Models, Coastal Estuarine Sci.* vol. 4, edited by N. Heaps, pp. 1-16, AGU, Washington, D.C., 1987.

De Madron, X. D., and G. L. Weatherly, Circulation, transport and bottom boundary layers of the deep currents in the Brazil Basin, *J. Mar. Res.*, *52*, 583-638, 1994.

Ezer, T., and G. L. Weatherly, A numerical study of the interaction between a deep cold jet and the bottom boundary layer of the ocean, *J. Phys. Oceanogr.*, *20*, 801-816, 1990.

Garrett, C., Marginal mixing theories, *Atmos. Ocean*, *29*, 313-339, 1991.

Garrett, C., P. MacCready, and P. Rhines, Boundary mixing and arrested Ekman layers: Rotating stratified flow near a sloping boundary, *Annu. Rev. Fluid Mech.*, *29*, 313-339, 1993.

Gill, A. E., The hydraulics of rotating-channel flow, *J. Fluid Mech.*, *80*, 641-671, 1977.

Hogg, N., P. Biscaye, W. Gardner, and W. J. Schmitz Jr., On the modification of Antarctic Bottom Water in the Vema Channel, *J. Mar. Res.*, *40*, suppl., 231-263, 1982.

Hogg, N. G., Hydraulic control and flow separation in a multi-layered fluid with application to the Vema Channel, *J. Phys. Oceanogr.*, *13*, 695-708, 1983.

Hogg, N. G., G. Siedler, and W. Zenk, Circulation and variability at the southern boundary of the Brazil Basin, J. Phys. Oceanogr., in press, 1999.

Johnson, D. A., The Vema Channel: Physiography, structure, and sediment - current interactions, *Mar. Geol.*, *58*, 1-34, 1984.

Johnson, D. A., S. E. Mc Dowell, L. G. Sullivan, and P. E. Biscaye, Abyssal hydrography, nephelometry, currents, and benthic boundary layer structure in the Vema Channel, *J. Geophys. Res.*, *81*, 5771-5786, 1976.

Johnson, G. C., and D. R. Ohlsen, Frictionally modified rotating hydraulic channel exchange and ocean outflows, *J. Phys. Oceanogr.*, *24*, 66-78, 1994.

Johnson, G. C., and T. B. Sanford, Secondary circulation in the Faroe Bank Channel outflow, *J. Phys. Oceanogr.*, *22*, 927-933, 1992.

Killworth, P. D., Flow properties in rotating, stratified hydraulics, *J. Phys. Oceanogr.*, *22*, 997-1017, 1992.

MacCready, P., and P. Rhines, Buoyant inhibition of Ekman transport on a slope and its effect on stratified spin-up, *J. Fluid Mech.*, *223*, 631-661, 1991.

MacCready, P., and P. Rhines, Slippery bottom layers on a slope, *J. Phys. Oceanogr.*, *23*, 5-22, 1993.

Marshall, J., C. Hill, L. Perelman, and A. Adcroft, Hydrostatic, quasi-hydrostatic, and nonhydrostatic ocean modeling, *J. Geophys. Res.*, *102*, 5733-5752, 1997.

Mellor, G. L., Numerical simulation and analysis of the mean coastal circulation off California, *Cont. Shelf Res.*, *6*, 689-713, 1986.

Mellor, G. L., and X. H. Wang, Pressure compensation and the bottom boundary layer, *J. Phys. Oceanogr.*, *26*, 2214 - 2222, 1996.

Mellor, G. L. and T. Yamada, Development of a turbulence closure model for geophysical fluid problems, *Rev. Geophys, 20*, 851-875, 1982.

Middleton, J. F., and D. Ramsden, The evolution of the bottom boundary layer on the sloping continental shelf: A numerical study, *J. Geophys. Res., 101*, 18,061-18,077, 1996.

Onken, R., The spreading of Lower Circumpolar Deep Water in the Atlantic Ocean, *J. Phys. Oceanogr.*, *25*, 3051-3063, 1995.

Reid, J. L., W. D. Nowlin Jr., and W. C. Patzert, On the characteristics and circulation of the southwestern Atlantic Ocean, *J. Phys. Oceanogr.*, *7*, 62-91, 1977.

Sarmiento, J. L., W. S. Broecker, and P. E. Biscaye, Excess bottom radon 222 distribution in deep ocean passages, *J. Geophys. Res.*, *83*, 5068-5076, 1978.

Siedler, G., and W. Zenk, WOCE Südatlantik 1991, Reise Nr. 15, 30. Dez. 1990-23. März 1991, *Meteor-Ber.*, *92*(1), 126 pp, Univ. Hamburg, Hamburg, Germany, 1992.

Speer, K. G., and W. Zenk, The flow of Antarctic bottom water into the Brazil Basin, *J. Phys. Oceanogr.*, *23*, 2667-2682, 1993.

Trowbridge, J. H., and S. J. Lentz, Asymmetric behavior of an oceanic boundary layer above a sloping bottom, *J. Phys. Oceanogr.*, *21*, 1171-1185, 1991.

Weaterly, G. L., and P. J. Martin, On the structure and dynamics of the oceanic bottom boundary layer, *J. Phys. Oceanogr.*, *8*, 557-570, 1978.

Whitehead, J. A., Internal hydraulic control in rotating fluids - Applications to oceans, Geophys. Astrophys. Fluid Dynamics, *48*, 169-192, 1989.

Whitehead, J. A., A. Leetma, and R. A. Knox, Rotating hydraulics of strait and sill flows, *Geophys. Fluid. Dyn.*, *6*, 101-125, 1974.

Wright, W. R., Northward transport of Antarctic Bottom Water in the western Atlantic Ocean, *Deep Sea Res.*, *17*, 367-371, 1970.

Wüst, G., Das Bodenwasser und die Gliederung der Atlantischen Tiefsee, *Wissenschaftliche Ergebnisse der Deutschen Atlantischen Expedition auf dem Forschungs- und Vermessungsschiff „Meteor" 1925-1927*, Band VI, Teil 1, pp. 1-107, Walther de Gruyter, Berlin, 1933.

Zenk, W., K. G. Speer, and N. G. Hogg, Bathymetry at the Vema Sill, *Deep Sea Res.*, Part I, *40*, 1925-1933, 1993.

J. H. Jungclaus and M. Vanicek, Institut für Meereskunde an der Universität Kiel, Düsternbrooker Weg 20, 24105 Kiel, Germany. (email: jjungclaus@ifm.uni-kiel.de; mvanicek@ifm.uni-kiel.de.)

(Received February 16, 1998; revised September 14, 1998; accepted October 23, 1998.)